ACS APPLIED MATERIALS & INTERFACES

RESEARCH ARTICLE

www.acsami.org

Electronic and Magnetic Properties and Structural Stability of BeO Sheet and Nanoribbons

Wenzhi Wu, Peng Lu, Zhuhua Zhang,* and Wanlin Guo*

Institute of Nano Science, State Key Laboratory of Mechanics and Control of Mechanical Structures and Key Laboratory for Intelligent Nano Materials and Devices of the Ministry of Education, Nanjing University of Aeronautics and Astronautics, Nanjing 210016, China

ABSTRACT: The novel electronic and magnetic properties of BeO nanoribbons (BeO NRs) as well as their stability are investigated through extensive density functional theory calculations. Different from semiconducting graphene nanoribbons and insulating BN ribbons, all zigzag edged BeO NRs are revealed to display ferromagnetic and metallic natures independent of the ribbon width and edge passivation. The polarized electron spins in H-passivated zigzag BeO NRs are from the unpaired electrons around the weakly formed Be−H bonds, while those of bare zigzag BeO NRs are due to the 2p states of edge O atoms. In sharp contrast, all armchair BeO NRs are nonmagnetic insulators regardless of the edge passivation. In particular, all bare armchair BeO NRs have a nearly constant band gap due to a peculiar edge localization effect. Interestingly, the band gaps of all armchair BeO NRs can be markedly reduced by an applied transverse electric field and even completely closed at a critical field. The critical electric field required for gap closing decreases with increasing ribbon width, thus the results have practical importance. Further stability analysis shows that bare BeO NRs are more stable than H-passivated BeO NRs of similar ribbon widths and bare armchair BeO NRs are energetically the most favorable among all the nanoribbons.

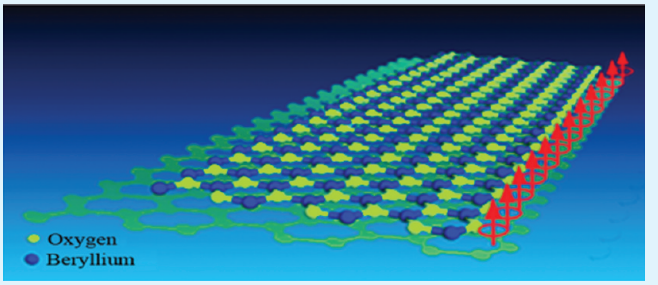

KEYWORDS: BeO, sheet, nanoribbons, electronic structure, magnetism, stability

1. INTRODUCTION

Since the discovery of carbon nanotubes (CNTs),[1] low-dimensional nanostructures such as nanotubes, nanowires, nanoribbons, and nanosheets have been intensively studied in an effort to understand their novel structural and electronic properties and to explore their potential applications for a wide range of novel devices. In particular, graphene, a two-dimensional (2D) honeycomb structure of carbon, has been the new star of condensed matter physics.[2] Because of its unique symmetry and single-atom thickness, electron and hole bands of graphene show linear crossing at the Fermi level,[3] resulting in a massless Dirac fermionlike behavior of charge carriers. With this band feature, versatile properties such as the Klein paradox,[4,5] the anomalous quantum Hall effect,[6,7] and high mobility even at room temperature appear in graphene, which open exciting prospect of finding applications in high-performance electronic devices. Besides 2D graphene, its quasi-one-dimensional (1D) graphene nanoribbons (GNRs) have also undergone a flurry of research interest since they possess more ample electronic and magnetic properties.[8−15] Most notably, GNRs with zigzag edges are predicted to be antiferromagnetic (AFM) semiconductors,[9] where the polarized electron spins are ferromagnetically aligned along the ribbon edges and antiferromagnetically coupled between the two opposite edges. Such an amazing spin ordering can give rise to many unusual properties such as half metallicity,[10] giant magnetoresistance effect,[11] and magnetoelectric effect[12] with promising applications. These studies on graphene-based materials have sparked considerable researches into other hexagonal materials of monatomic layer in thickness, such as BN,[16−19] SiC,[20] ZnO,[21] GaN,[22] MoS_2,[23] and their corresponding nanoribbons and nanosheets. These monolayer compound materials are even more interesting in their exotic electronic characters and widely variable electronic properties according to the atomic stoichiometry at their edges. However, a great research interest is still going on predicting new monatomic-layer crystals and their derivatives.

As an exceptional member of the series of alkaline-earth oxides, beryllium oxide (BeO) is the only material crystallizing in the wurtzite lattice rather than in the cubic sodium chloride structure. This can be attributed to a significant covalent component in the primarily ionic Be−O bond, as revealed by Compton scattering measurements.[24] This distinct bonding feature in BeO gives rise to fascinating mechanical and physical properties, such as high hardness, melting point and thermal conductivity as well as large elastic constants. Because of its large experimental band gap up to 10.7 eV, BeO has been widely used in current industrial instruments, including refractory material in metallurgy and protective coatings, heat-removing insulators and a reflector for neutrons and neutron filters. Moreover, BeO is also often used in laser engineering, ionizing radiation dosimetry, microwave radio-engineering devices, and a variety of nanodevices.[25−29] Considering these powerful applications, a number of studies have been devoted to exploring new possible structural phases for BeO. It is found that high-pressure and high-temperature conditions can

Received: September 21, 2011
Accepted: October 31, 2011
Published: October 31, 2011

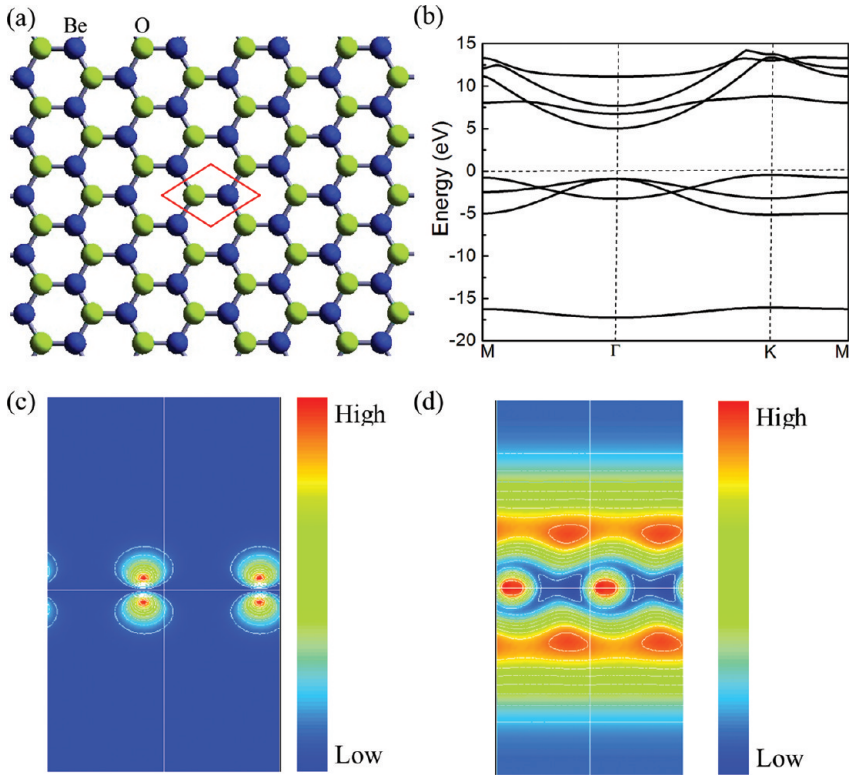

Figure 1. (a) Atomic and (b) band structures of a monolayer *h*-BeO sheet. (c) Charge density contours of the VBM and CBM states of the BeO sheet. The rhombus represents a unit cell of BeO sheet. The lime balls denote oxygen atoms, and the navy blue balls represent beryllium atoms.

transform BeO into insulating rocksalt[30] and tetragonal β-beryllia[31] structures, respectively. In particular, Continenza et al.[32] predicted theoretically the existence of the hexagonal BeO compound (*h*-BeO or BeO sheet) in which the beryllium and oxygen atoms are bonded together by sp^2 hybridized bonds, as do the other members of the isoelectronic series of the first-row elements (e.g., graphite and hexagonal BN). Ijchanot et al.[33] studied the relative stability of the dense wurtzite and hexagonal phases of BeO along the transformation pathway from the wurtzite to the hexagonal phase, showing that *h*-BeO is less stable with respect to the wurtzite phase. Sorokin et al.[27] made a systematic study on the binding energies of the BeO structures with different morphologies, including BeO molecules, wurtzite-type structures, monolayer hexagonal sheets, and nanotubes. They show that the layered phase of BeO is energetically likely to exist in free space. Following these studies, the structures of pristine BeO nanotubes (BeO NTs) were recently predicted, with their structural, elastic, and electronic properties being comprehensively studied.[29,33] The results show that the BeO NTs are wide-band-gap compounds and their band gaps are insensitive to helicity, which are somewhat different from SiC and BN NTs.[29] In addition, it is also revealed that the structural and elastic properties of BeO NTs are largely independent of NT helicity[29] and their Young's modulus are comparable to that of the CNTs.[33] Because of these excellent mechanical properties, Gorbunova et al.[34] have attempted to explore the electronic properties and magnetism in BeO NTs induced by nonmagnetic sp impurities (i.e., boron, carbon, and nitrogen) as well as by vacancy defects. This study shows a possibility for doped and defective BeO NTs to be used in spintronic devices. Even so, the monolayer BeO sheet has received little research attention. Especially, motivated by the novel physical phenomena from the edge of graphene, a question arises naturally as to what would happen at the edges of monolayer *h*-BeO. In view of the large difference between the electron negativities of Be and O, the edge states of the BeO sheet should be significantly different from those of graphene and other compound monolayer. In this regard, BeO nanoribbons (BeO NRs) with different edge shapes and passivations are worthy of particular investigations, which is of high relevance to practical applications since fabricating nanoribbons from the seamless nanotubes and 2D sheets is well within the reach of current experimental techniques, as it has been done for yielding GNRs.[35] However, to the best of our knowledge, the structural, electronic, and magnetic properties of BeO NRs remain unexplored, despite so much attention paid to BeO NTs.[24−34]

In this study, we perform a systematical first-principles investigation on the structural stability, electronic, and magnetic properties of the 2D BeO sheet and 1D BeO NRs. It is found that the BeO NRs exhibit many unique electronic and magnetic properties remarkably different from those of GNRs and BN NRs. All the zigzag BeO nanoribbons (Z-BeO NRs) exhibit ferromagnetic and metallic behaviors, which are robust to the edge passivation. Quite differently, all the bare and H-passivated armchair BeO nanoribbons (A-BeO NRs) are always nonmagnetic insulator, showing different width dependence of band gap for nanoribbons with and without edge passivation. A remarkable feature for all the insulating A-BeO NRs is that their band gaps can be markedly reduced by a transverse electric field and even completely closed when the electric field is over a critical value. All these NRs are thermodynamically stable, and the bare A-BeO NRs are distinctly more stable over other types of BeO NRs. Our results suggest that BeO NRs can be new candidates for future nanoelectronics and spintronics applications.

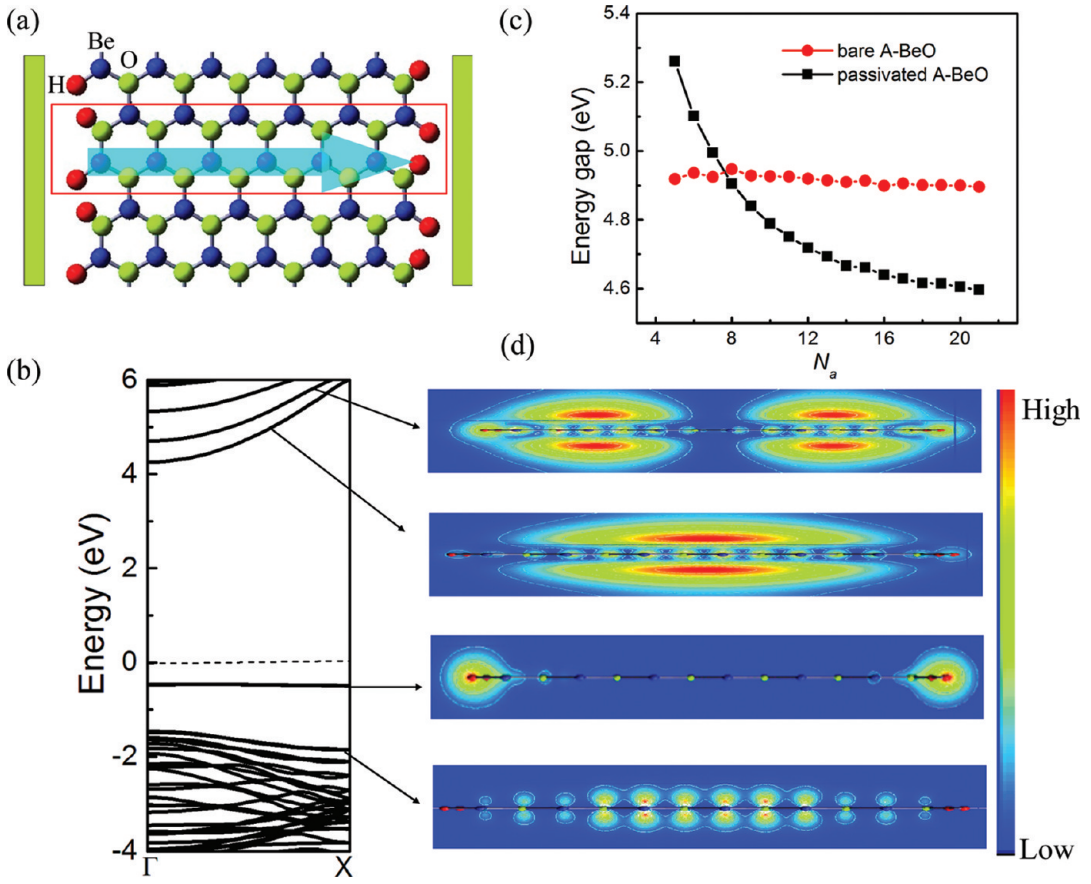

Figure 2. (a) Atomic structure with primitive unit cell delineated and (b) band structure of H-passivated 12-A-BeO NR. The longitudinal direction is the infinitely extended direction. The Fermi level is set to zero. (c) Variation in band gaps of H-passivated N_a-A-BeO NRs (black line) and bare N_a-A-BeO NRs (red curve) as a function of width. (d) Charge densities of selected specific states of H-passivated 12-A-BeO NR. The positive direction of E_{ext} is denoted by a big arrow in Figure 2a for subsequent discussions. The navy blue, lime, and red balls denote beryllium, oxygen and hydrogen atoms, respectively.

2. COMPUTATIONAL METHOD

The calculations are performed within the framework of density-functional theory as implemented in the Vienna ab initio simulation package (VASP).[36] Core and valence electrons are described using the ultrasoft pseudopotentials.[37] Electron exchange and correlation is treated using the local (spin) density approximation (LSDA). Test calculations using the generalized gradient approximation (GGA) give almost the same results. A kinetic-energy cutoff of 494.6 eV is used in the plane-wave expansion. The conjugate gradient method is used to optimize the geometry and all the atoms in the unit cell are fully relaxed until the force on each atom is less than 0.01 eV/Å. Electronic minimization was performed with a tolerance of 10^{-5} eV. For all BeO NRs, the Brillouin-zone integration is sampled by up to 20 Monkhorst-Pack special k points for atomic structure relaxation and a total of 50 k points for electronic-structure calculation. A 12×12×1 Monkhorst-Pack k-points grid is used for the BeO sheet. A one-dimensional periodic boundary condition is applied along the ribbon edge. Both of the distances between edges and between planes of two adjacent ribbons are at least 10 Å, which is large enough to eliminate the effect of direct ribbon−ribbon interaction. The external electric field is introduced by the planar dipole layer method as implemented in VASP.[38]

3. RESULTS AND DISCUSSION

3.1. Electronic Properties of 2D Hexagonal BeO sheet. We first examine the structure of 2D *h*-BeO sheet, as shown in Figure 1. The optimized Be−O bond length is 1.525 Å, which is in agreement with previous calculations.[29] The computed binding energy of the BeO sheet is 6.846 eV/atom, lower than the 7.07 eV/atom of wurtzite BeO. The electronic band structure of BeO sheet is shown in Figure 1b. We can find that the *h*-BeO sheet is a large-gap semiconductor with an indirect band gap of 5.45 eV, which is well consistent with the gap value of previous DFT results.[29,32,33] Here, we should state that the common DFT calculation underestimates the energy gap. An accurate first-principles calculation of band gaps requires a quasiparticle approach (GW); however, the basic physics discovered here should not be changed. It is found that the conduction band minimum (CBM) of *h*-BeO sheet is located at Γ point, while the valence band maximum (VBM) lies at vertice K. To understand the energy gap, the electron densities corresponding to the CBM and VBM states are plotted in Figures 1c and 1d, respectively. The VBM state displays a character of O $2p_z$ orbital and the charge density is highly localized on the O atoms, shaped as a π state; whereas the CBM state has the O s character and actually shows a dispersion feature of the nearly free-electron (NFE) state, which exists in many layered structures, such as hexagonal BN sheet.[16] We also identify the π^* states located on the B atoms, which are higher in energy over the CBM. This band feature is distinct to those of the graphene and BN sheets, where the CBM is contributed by the π^* states which are lower in energy than the NFE states. The remarkably dropped NFE states with respect to

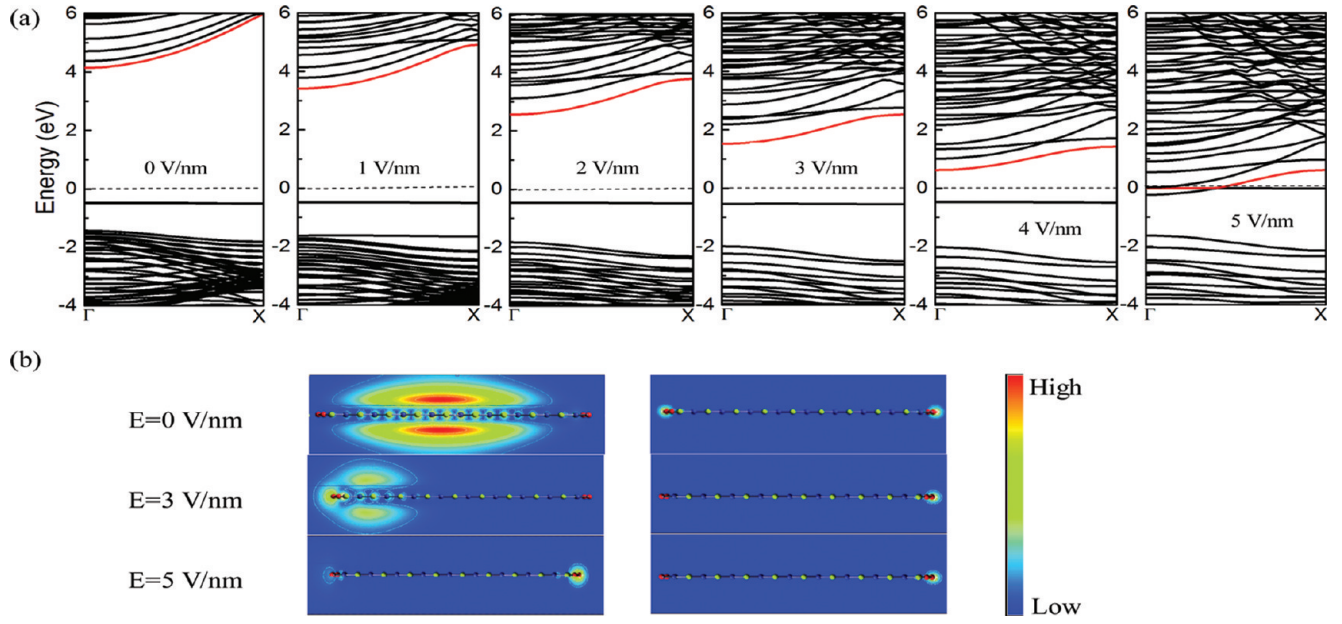

Figure 3. Effects of positive electric field on the electronic structures of H-passivated A-BeO NRs. In all figures, the Fermi level is set to zero and the NFE band is guided to eyes by a red line. (a) Band structure of H-passivated 18-A-BeO NR at E_{ext} = 0, 1, 2, 3, 4, and 5 V/nm. (b) Charge densities of the lowest conduction band (the left panel) and the highest valence band (the right panel) at E_{ext} = 0, 3, and 5 V/nm.

the π^* states can pose an important influence on the electronic properties and transport in the BeO sheet and will bring up different electric field effects in BeO NRs, which will be addressed below.

3.2. Electronic Properties of Armchair BeO Nanoribbons. We now address the structure and electronic properties of BeO NRs. Similar to GNRs, we consider two typically shaped edges for the BeO NRs, i.e. armchair and zigzag, respectively, with which the corresponding nanoribbons are denoted as A-BeO NRs and Z-BeO NRs. Both kinds of nanoribbons can be cut from the single-layer *h*-BeO sheet along respective crystallographic orientations. Following the convention, we use the notation N_a-A-BeO NRs to describe an A-BeO NRs having N_a Be−O dimer lines across the ribbon width and use N_z-Z-BeO NRs to describe a Z-BeO NRs having N_z zigzag Be−O chains, as shown in Figures 2a and 6a, respectively. We first terminate all the edge Be and O atoms with H atoms to remove the effect of dangling bonds.

In what follows, we explore the structural and electronic properties of H-passivated A-BeO NRs. The optimized atomic structure of the H-passivated 12-A-BeO NR is shown in Figure 2a. As mentioned above, the edge atoms are terminated with H atoms, so the bond characters and the on-site energies of Be and O atoms at the edges are different from those in the interior of the A-BeO NRs. This changes the Be−O bonding length around the ribbon edges. In order to determine the ground state of the A-BeO NRs, we perform total energy calculations for the spin-unpolarized and spin-polarized states, respectively, and do not find any energy difference between them, indicative of a non-magnetic system. The band structure of the H-passivated 12-A-BeO NR is plotted in Figure 2b, together with the isosurface plots of partial charge densities for several denoted bands in Figure 2d. A direct band gap of 4.72 eV (LDA value) is formed between the VBM and CBM at Brillouin-zone center Γ point. The highest valence band is double-degenerate and mainly contributed by the H atoms connecting with O atoms, which is highly localized; while the lowest conduction band is non-degenerate and contributed by the aforementioned NFE states that are weakly bound to the ribbon plane. Further charge density analyses show that the state associated with the second lowest conduction band is also a NFE state and distributes mainly around the two ribbon edges, whereas the second highest valence band is almost uniformly distributed on O atoms throughout the ribbon width except for the edge O atoms. The near-gap conduction states in the A-BeO NRs will show sensitive changes to external potential perturbation because they are weakly bound to atomic framework of the ribbons.

Through extensive computation of the band structures for a series of H-passivated A-BeO NRs, we obtain the variation in the band gap E_g for the H-passivated A-BeO NRs as a function of ribbon width (namely, N_a), as shown in Figure 2c. The band gap of H-passivated A-BeO NRs decreases monotonically with increasing ribbon width. This is in contrast to the case of armchair GNRs[14] and BN NRs,[19] where three distinct families of behaviors are distinctly present. Nevertheless, this behavior is akin to the case of armchair ZnO NRs,[39] suggesting different behavior of confinement effect in layered-oxide nanoribbons. This is due to the presence of a highly localized band below the Fermi level that is unvaried with ribbon width. Such a band is produced mainly by the edge effect and hence less sensitive to the quantum confinement. We also note that the energy gap does not converge to that of BeO sheet as the width increases, just due to such highly localized highest valence band.

The above results have established that the H-passivated A-BeO NR is an insulator regardless of its width because of the large energy gap and its finite variations versus ribbon width. However, for applications, it is more desirable to realize a widely tunable band gap in the BeO NRs as it would allow great flexibility in design and optimization of nanodevices, in particular if it could be tuned by applying a well-controlled external electric field. We thus turn to investigating the energy gap modulation of the H-passivated A-BeO NRs using an external transverse electric field (E_{ext}). Here we define the positive direction of the applied electric field by a big arrow, as illustrated in Figure 2a. Figure 3a

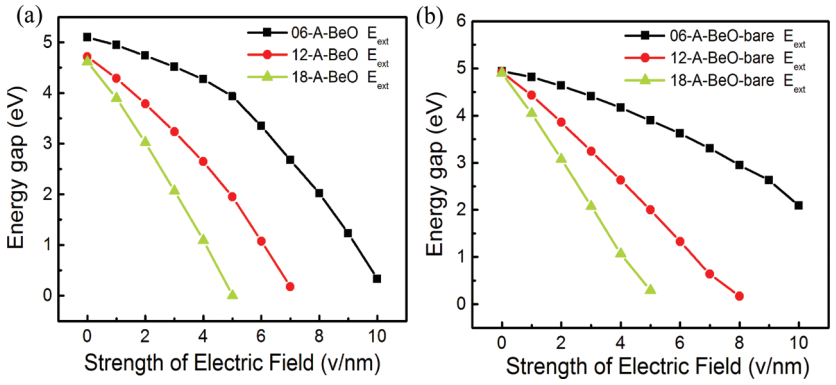

Figure 4. Dependence of the gap modulation of (a) H-passivated and (b) bare A-BeO NRs on the size of width under the transverse electric field.

shows the band structures of H-passivated 18-A-BeO NR under different positive E_{ext}. It is clearly shown that the band gap is markedly reduced with increasing E_{ext} and is eventually closed when E_{ext} reaches a critical value of 5 V/nm. To investigate the underlying physical mechanism, we plot the charge densities for the lowest conduction band and the highest valence band in the 18-A-BeO NR at E_{ext} = 0, 3, and 5 V/nm, as shown in Figure 3b. At zero field, the charge density for the lowest conduction band is localized at O atoms throughout the ribbon, as has been illustrated above; whereas the charge density for the highest valence band is found to be mainly localized at H atoms connecting with O atoms. When E_{ext} = 3 V/nm, the lowest conduction band downshifts remarkably since it is from the weakly bound NFE states and is easily redistributed in response to the electric field, while the highest valence band also slightly upshifts in energy toward the Fermi level. This is unique in BeO NRs because the NFE states in other systems are usually located higher in energy than the tightly bound π^* state. As a result, the band gap of the nanoribbon is reduced much more rapidly, especially in the region of low field strength, which is of high relevance to technological application. As the electric field increases, the charge densities of the lowest conduction band and the highest valence band localize at the opposite edges, where the external electrostatic potential felt by an electron is increased and decreased, respectively, thereby further narrowing the band gap. Consequently, the energy gap of the H-passivated 18-A-BeO NR is closed at merely E_{ext} = 5 V/nm. No distinct difference is found when the electric field direction is reversed, owing to the symmetrical structure in A-BeO NRs. Importantly, the gap modulation of the H-passivated A-BeO NRs induced by the transverse electric field is also width-dependent, like that in BN NRs.[39] As shown in Figure 4a, the field-induced gap modulation is more pronounced in wider ribbon and the critical field strength will decrease dramatically with further increasing ribbon width. The width dependence can be explained by the field-induced electrostatic potential difference between the two ribbon edges, which is proportional to the size of the H-passivated A-BeO NR. Due to the limits of computational ability, the range of the ribbon width included in the present investigations is limited to 2.44 nm for the H-passivated 18-A-BeO NR, and the critical electric field needed to close its band gap is high and seems to be difficult to achieve in laboratory. Nevertheless, the trend shown in Figure 4a renders it possible to realize the gap closure at the commonly achievable field strengths when the ribbon width is sufficiently wide. In fact, the ribbon width obtained in experiments usually reaches up to tens or even hundreds of nanometers, which would make the band gap sensitively modulated by an electric field available in practice. The sensitive field-induced band gap modulation makes the H-passivated A-BeO NR suitable for diverse applications in nanodevices.

To distinguish the effect of edge passivations, we also studied the structure and electronic properties of bare A-BeO NRs. Unlike the three-fold coordination in the *h*-BeO sheet, each Be or O atom at the edges of bare A-BeO NRs is only two-fold coordinated. The optimized atomic structure of bare 18-A-BeO NR is shown in Figure 5a, where the atoms at the edges of the bare A-BeO NRs undergo a significant buckling with the edge Be and O atoms displaced inward and outward with respect to the ribbon edge, respectively. It is found that all the bare A-BeO NRs involved in our calculations exhibit a semiconducting nature with direct band gaps. Interestingly, the band gap is essentially unchanged with varying ribbon width and remains nearly constant around 4.90 eV (see Figure 2c).

The energy gap modulation of the bare A-BeO NRs by a transverse electric field is also examined. Figure 4b shows the evolution of the band gaps of bare A-BeO NRs with different widths under external electric fields. The band gaps of bare A-BeO NRs show remarkable width-dependent modulation by the electric field, similar to the H-passivated A-BeO NRs. To understand this behavior, we examined the field-induced influence on the nearly-gap electronic states of bare A-BeO NRs as well. Figure 5c exhibits the plots of charge densities for the lowest conduction band and the highest valence band in the bare 18-A-BeO NR at E_{ext} = 0, 3, and 5 V/nm, respectively. It is found that the charge distributions of the lowest conduction band and the highest valence band are different from those of the corresponding H-passivated systems. At zero field, the charge density analyses demonstrate that the highest valence band is an edge state with wave function localized at the edge O atoms, whereas the lowest conduction band is a localized state, with its wave function being more loosely distributed around the edge Be atoms. This charge distribution determines that the band gap will not change remarkably with ribbon width because all the near-gap states are entirely from an edge effect and not from the well-known quantum confinement effect. When an external electric field of 3 V/nm is applied (Figure 5c), the charge distributions of the lowest conduction band and the highest valence band are driven to redistribute at opposite edges owing to the change in electrostatic potential, as analyzed above. This charge redistribution reduces band gaps in bare A-BeO NR, with nearly the same slope as that shown in Figure 4a for the H-passivated ribbons. The widely tunable band gap modulations in both H-passivated and bare

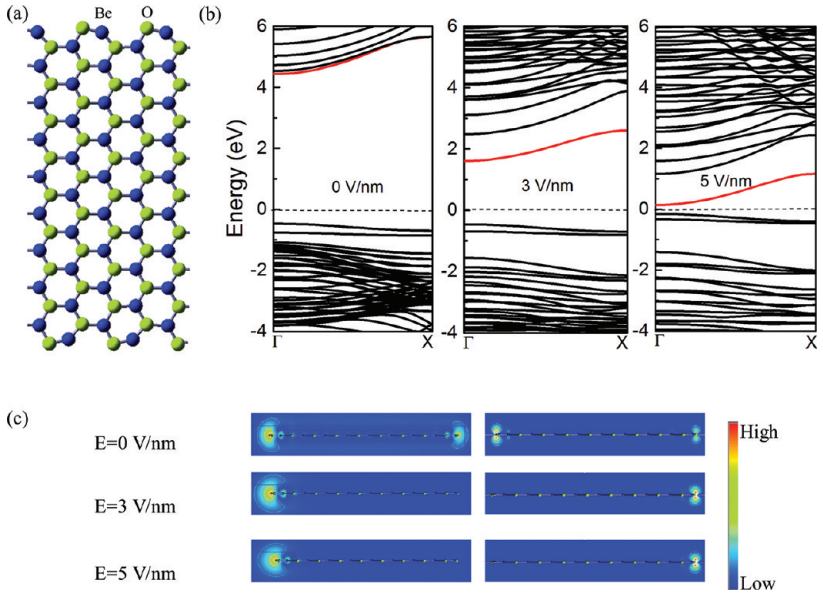

Figure 5. (a) Atomic and (b) band structures of bare 18-A-BeO NR at E_{ext} = 0, 3, and 5 V/nm. (c) Charge densities of the lowest conduction band (the left panel) and the highest valence band (the right panel) at E_{ext} = 0, 3, and 5 V/nm.

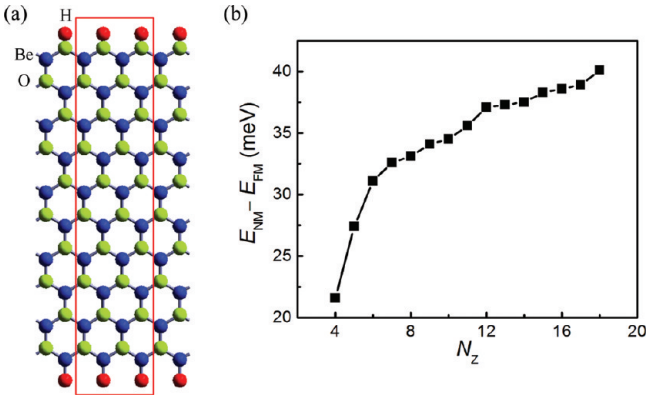

Figure 6. (a) Atomic structure of H-passivated 10-Z-BeO NR with primitive double cell delineated. (b) The variation of relative energies of ferromagnetic (FM), and nonmagnetic (NM) states of H-passivated N_z-Z-BeO NRs as a function of width.

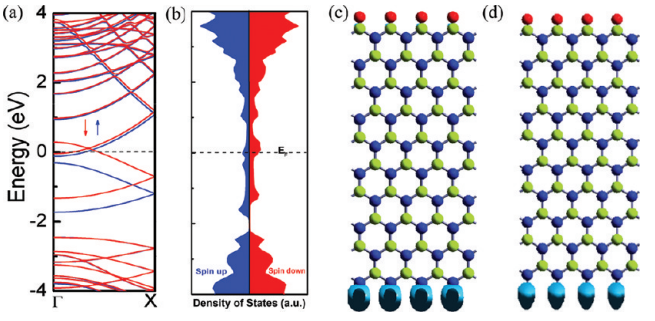

Figure 7. (a) Band structure, (b) total density of spin-up and spin-down states (DOS), (c) spatial spin density distribution ($\rho_\uparrow$-$\rho_\downarrow$), and (d) electron localization function (ELF) plots with an isosurface value of 0.8 of the H-passivated 10-Z-BeO.

A-BeO NRs confirm the robustness of the band engineering by electric fields.

3.3. Electronic and Magnetic Properties of Zigzag BeO Nanoribbons. We now explore the electronic and magnetic properties of H-passivated Z-BeO NRs. We first take the H-passivated 10-Z-BeO as a prototype model for discussion. Figure 6a displays the optimized atomic structure of the H-passivated 10-Z-BeO NR with a width of 21.42 Å. During the structure optimization, we have performed both spin-unpolarized and spin-polarized computations to determine the ground state of Z-BeO NRs. To realize the antiferromagnetic (AFM) order at the edges, we also consider a double periodicity unit cell so that two Be atoms and two O atoms are included at the opposite edges, respectively. This allows us to study six possible spin configurations for Z-BeO NRs according to the spin directions (spin-up or spin-down) on the Be and O edges. They are denoted as Be(++)/O(++), Be(++)/O(+−), Be(++)/O(−−), Be(+−)/O(++), Be(+−)/O(+−), and Be(+−)/O(−+). Here, Be and O indicate the edge Be and O atoms, and the + and − in the parentheses represent the spin-up and spin-down, respectively. We perform total energy calculations for the 10-Z-BeO NR with the six above-mentioned spin configurations. Interestingly, all the spin configurations converge to two magnetic solutions: The first four spin configurations converge to the same ferromagnetic (FM) solution and the magnetization density is concentrated at the Be-edge of the ribbon; whereas the last two spin configurations converge to the nonmagnetic (NM) solution. We find that the ferromagnetic state corresponds to the ground state of the H-passivated 10-Z-BeO NR with its total energy lower than the nonmagnetic states by 34.5 meV per/supercell.

The spin-polarized band structures for the H-passivated 10-Z-BeO NR are shown in Figure 7. The states of opposite spin orientation are not degenerate around the Fermi level and both spin channels show a metallic feature. Moreover, the metallic character is independent of the ribbon width. To obtain further insight, we plot the atom-resolved total density of states of H-passivated 10-Z-BeO NR, as shown in Figure 7b. The states near the Fermi

levels in both spin channels are mostly from the 2p state of the edge Be atoms and 1s state of the H atoms, which is consistent with the results of spatial spin density distribution shown in Figure 7, where we find that the major contribution to the states at the Fermi level is due to the Be-terminated edge. The magnetism of H-passivated Z-BeO NRs is similar to theoretical predictions reported in zigzag ZnO NRs,[40] but is markedly different from the zigzag GNRs whose two edges are antiferromagnetically coupled and also from the zigzag MoS_2 NRs whose two edges are ferromagnetically coupled.[23] To further clarify the origin of the polarized spins, we plot the electron localization function (ELF) for H-passivated 10-Z-BeO NR with an isosurface value of 0.80 in Figure 7d, where the strong localization is observed around H atoms at the Be edge. Such a localized state is due to the weak Be−H bond strength, so electrons of the Be and H atoms do not tend to participate in forming strong covalent bonds but act as unpaired electrons to favor the spin polarization. Indeed, we find the magnetism in the 10-Z-BeO NR is quenched upon terminating the Be edge with F atom that has higher electronegativity.

For all the H-passivated Z-BeO NRs studied in this work, the FM state lies in the ground state since the spin-polarized total energies are always lower than the spin-unpolarized ones, as evidenced in Figure 6b. The calculated energy difference (ΔE) between the FM state and NM states increases with the increasing ribbon width, indicating enhanced stability of the FM state in wider Z-BeO NRs. Nevertheless, the total magnetic moment per double cell remains approximately constant at the value of $0.13\mu_B$, regardless of the ribbon width. Because the magnetic moment is mostly distributed around the Be-terminated edge, we hope that the magnetism of Z-BeO NRs is still appreciable in the ribbons of common experimental size.

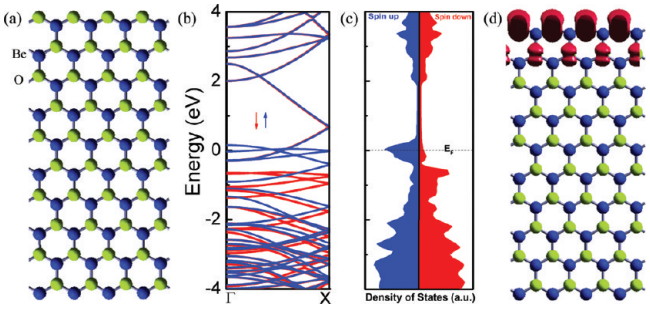

Figure 8. (a) Atomic, (b) band structure, (c) total densities of spin-up and spin-down states, and (d) spatial spin density distribution ($\rho_\uparrow - \rho_\downarrow$) of bare 10-Z-BeO NR.

We also investigate the structure and electronic properties of bare Z-BeO NRs to evaluate the effect of edge termination. Still, we use the bare 10-Z-BeO NR as a model system to demonstrate our results. Figure 8a displays the optimized atomic structure of the bare 10-Z-BeO NR. It is shown that the bare 10-Z-BeO NR retains the planar configuration and edge distortion is not observed. Both spin-unpolarized and spin-polarized computations have been carried out during the structural optimization. It is found that the bare 10-Z-BeO NR also has a ferromagnetic ground state, which is 151 meV lower in total energy than that obtained from spin-unpolarized calculations. The total magnetic moment of the bare 10-Z-BeO NR can now be up to $0.78\mu_B$ per double cell, which is larger than the moment of $0.13\mu_B$ in the H-passivated 10-Z-BeO NR. Figure 8b shows spin-polarized band structure of bare 10-Z-BeO NR. It is found that the spin-splitting mainly happens in the valence band, in particular in those close to the Fermi level, while all the conduction bands are spin degenerate. Note that both spin channels show a metallic feature, rendering the bare 10-Z-BeO NR a FM metallic wire. There are three bands of the spin-down channel crossing the Fermi level but only one band in spin-down channel cuts the Fermi level, giving rise to a large spin-polarization at the Fermi level. The atomic-resolved DOS reveals that the spin-polarized states are mostly from the edge O atoms. This is further corroborated by the magnetization density distribution as illustrated in Figures 8d, where the polarized spins are mainly from the edge O atoms and show a rapid decay in magnitude into the ribbon interiors. This is because the edge O atoms in the bare NR have one unpaired electron, which is easily spin-polarized due to the large spin exchange interaction of O as well as the large density of states (DOS) near the VBM that are typical for all oxide compounds,[41] which is in contrast to the magnetic origin in H-passivated Z-BeO NRs.

We also discuss briefly the influence of the width on the electronic and magnetic properties of bare Z-BeO NRs. It is shown that bare N_z-Z-BeO NRs have similar electronic and magnetic properties ($N_z = 6-16$). By varying the ribbon width, the bare N_z-Z-BeO NRs can always keep metallic property, and they also have a ferromagnetic ground state with unpaired spins at the edges dominated by O atoms. In addition, we can see that total magnetic moment per double cell for a series of bare Z-BeO NRs increases gradually with increasing ribbon width. For example, the total magnetic moment of bare 6-Z-BeO NR is $0.46\mu_B$, which is increased to $0.81\mu_B$ for the bare 12-Z-BeO NR and to $0.84\mu_B$ for the bare 16-Z-BeO NR. This is crucial to the practical application of bare Z-BeO NRs in spintronics.

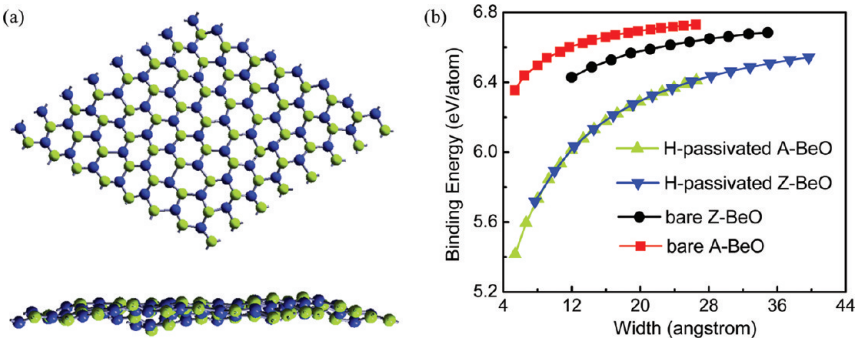

Figure 9. (a) Snapshots of the 2D *h*-BeO sheet at the end of a 5 ps ab initio molecular dynamical simulation at 2000 K. (b) Binding energy per atom of H-passivated A-BeO ($N_a = 5-21$), H-passivated Z-BeO ($N_z = 4-18$), bare A-BeO ($N_a = 5-21$), and bare Z-BeO ($N_z = 6-16$) as a function of the ribbon width.

3.4. Stabilities of BeO Nanoribbons. The evaluation of the relative stability of BeO NRs is important and determines whether these nanostructures can be realized experimentally. To this end, we first examine the stability of the *h*-BeO sheet using finite temperature ab initio molecular-dynamics (AIMD) calculations with time steps of 1 fs. To lift the constraints imposed by a small unit cell, we consider an 8 × 8 supercell of the *h*-BeO sheet and keep the temperature of the system at 2000 K for 5 ps. The honeycomb structure is not broken throughout the simulation although the structure has small out-of-plane rippling, as shown in Figure 9a. We are aware of that these calculations may not be conclusive because 5 ps is not sufficient to capture all the statistic rules, but this picture is the best that one can see from the exiguous window limited by the computational cost imposed by AIMD method.

We then examine the stability of BeO NRs by determining the binding energy per atom as a function of the ribbon width. Here the binding energy per atom is defined as $E_b = (n_{Be}E_{Be} + n_OE_O + n_HE_H - E_{NRs})/N$, where E_{Be}, E_O, and E_H are the atomic energies of Be, O, and H atoms, respectively, E_{NRs} is the total energy of BeO NRs, and n_{Be}, n_O, and n_H are the number of Be, O, and H, respectively. The stability of different ribbons and clusters can be evaluated with these binding energies; those with larger binding energies are more stable. As shown in Figure 9b, the binding energies increase monotonically with increasing ribbon widths for all kinds of BeO nanoribbons, indicating that the wider ribbon will be more stable. For those BeO NRs with the same number of atoms per unit cell, the binding energies of bare A-BeO NRs are slightly higher than those of Z-BeO NRs, such as bare 12-A-BeO NR (6.643 eV) vs 12-Z-BeO NR (6.631 eV), whereas the binding energies of H-passivated Z-BeO NRs are much higher than those of H-passivated A-BeO NRs, such as H-passivated 12-Z-BeO NR (6.405 eV) vs H-passivated 12-A-BeO NR (6.132 eV). For NRs with similar widths, the binding energies of bare BeO nanoribbons are higher than those of H-passivated BeO nanoribbons. Remarkably, bare A-BeO NRs have the largest binding energies over all other types of NRs, indicative of the highest stability. This is due to the pronounced atomic reconstruction occurred at the edges of bare A-BeO NRs. Such reconstruction can greatly enhance the stability of armchair edges. Upon hydrogen passivation, the relative stabilities of A-BeO and Z-BeO NRs are almost identical at the same ribbon width. The stability hierarchy of BeO NRs is summarized as follows: bare A-BeO NRs > bare Z-BeO NRs > H-passivated A-BeO NRs = H-passivated Z-BeO NRs. The weak Be−H bonds in the passivated BeO NRs are the origin of their weaker stability with respect to the bare BeO NRs.

4. CONCLUSION

In summary, we have shown by first-principles calculations that BeO NRs possess unique electronic and magnetic properties that are sharply different from those of commonly studied graphene and BN nanoribbons. It is found that the H-passivated and bare Z-BeO NRs exhibit ferromagnetic and metallic behavior independent of ribbon width, whereas the H-passivated and bare A-BeO NRs exhibit nonmagnetic and insulating behavior with different width-dependent band gap. The magnetism of H-passivated Z-BeO NRs is attributed to the unpaired electron from weak Be−H bonds and is robust to the ribbon width, whereas bare Z-BeO NR has its polarized spins localized on the edge oxygen atoms. Significantly, the band gaps of H-passivated and bare A-BeO NRs can be markedly reduced by a transverse electric field and even be closed at an electric field over a critical strength, which decreases with increasing ribbon width. Finally, we reveal that bare BeO NRs are more stable than those of H-passivated BeO NRs of similar widths, with the bare A-BeO NRs being energetically the most favorable. These rich varieties of electronic and magnetic properties in the BeO NRs make them useful in future nanoelectronics and spintronics applications.

AUTHOR INFORMATION

Corresponding Author

*E-mail: wlguo@nuaa.edu.cn (W.G.); chuwazhang@nuaa.edu.cn (Z.Z.).

ACKNOWLEDGMENT

This work is supported by the 973 Program (2007CB936204, 2012CB933403), National NSF (11172124, 10732040, 91023026), and Jiangsu Province NSF (BK2008042, BK2011722) of China and the NUAA Research Fund (4015-YAH10043), National and Jiangsu Postdoctoral Research Foundation (20110490132, 1002015B).

REFERENCES

(1) Iijima, S. *Nature* **1991**, *354*, 56.
(2) Novoselov, K. S.; Geim, A. K.; Morozov, S. V.; Jiang, D.; Zhang, Y.; Dubonos, S. V.; Grigorieva, I. V.; Firsov, A. A. *Science* **2004**, *306*, 666.
(3) Wallace, P. R. *Phys. Rev.* **1947**, *71*, 622.
(4) Katsnelson, M. I.; Novoselov, K. S.; Geim, A. K. *Nat. Phys.* **2006**, *2*, 620.
(5) Novoselov, K. S.; Geim, A. K.; Morozov, S. V.; Jiang, D.; Katsnelson, M. I.; Grigorieva, I. V.; Dubonos, S. V.; Firsov, A. A. *Nature* **2005**, *438*, 197.
(6) Berger, C.; Song, Z.; Li, T.; Li, X.; Ogbazghi, A. Y.; Feng, R.; Dai, Z.; Marchenkov, A. N.; Conrad, E. H.; First, P. N.; de Heer, W. A. *Science* **2006**, *312*, 1191.
(7) Zhang, Y.; Tan, Y.; Stormer, H. L.; Kim, P. *Nature* **2005**, *438*, 201.
(8) Fujita, M.; Wakabayashi, K.; Nakada, K.; Kusakabe, K. *J. Phys. Soc. Jpn.* **1996**, *65*, 1920.
(9) Son, Y. W.; Cohen, M. L.; Louie, S. G. *Phys. Rev. Lett.* **2006**, *97*, 216803.
(10) Son, Y. W.; Cohen, M. L.; Louie, S. G. *Nature* **2006**, *444*, 347.
(11) Kim, W. Y.; Kim, K. S. *Nat. Nanotechnol.* **2008**, *3*, 408.
(12) Zhang, Z.; Chen, C.; Guo, W. *Phys. Rev. Lett.* **2009**, *103*, 187204.
(13) Barone, V.; Hod, O.; Scuseria, G. E. *Nano Lett.* **2006**, *6*, 2748.
(14) Yang, L.; Park, C. H.; Son, Y. W.; Cohen, M. L.; Louie, S. G. *Phys. Rev. Lett.* **2007**, *99*, 186801.
(15) Han, M. Y.; Özyilmaz, B.; Zhang, Y.; Kim, P. *Phys. Rev. Lett.* **2007**, *98*, 206805.
(16) Rubio, A.; Corkill, J. L.; Cohen, M. L. *Phys. Rev. B* **1994**, *49*, 5081.
(17) Blase, X.; Rubio, A.; Louie, S. G.; Cohen, M. L. *Phys. Rev. B* **1995**, *51*, 6868.
(18) Park, C.H.; Louie, S. G. *Nano Lett.* **2008**, *8*, 2200.
(19) Zhang, Z.; Guo, W. *Phys. Rev. B* **2008**, *77*, 075403.
(20) Sun, L.; Li, Y.; Li, Z.; Li, Q.; Zhou, Z.; Chen, Z.; Yang, J.; Hou, J. G. *J. Chem. Phys.* **2008**, *129*, 174114.
(21) Botello-Méndez, A. R.; López-Urías, F.; Terrones, M.; Terrones, H. *Nano Lett.* **2008**, *8*, 1562.
(22) Li, H.; Dai, J.; Li, J.; Zhang, S.; Zhou, J.; Zhang, L.; Chu, W.; Chen, D.; Zhao, H.; Yang, J.; Wu, Z. *J. Phys. Chem. C* **2010**, *114*, 11390.
(23) Li, Y.; Zhou, Z.; Zhang, S.; Chen, Z. *J. Am. Chem. Soc.* **2008**, *130*, 16739.
(24) Joshi, K. B.; Jain, R.; Pandya, R. K.; Ahuja, B. L.; Sharma, B. K. *J. Chem. Phys.* **1999**, *111*, 163.
(25) Duman, S.; Sütlü, A.; Bağcı, S.; Tütüncü, H. M.; Srivastava, G. P. *J. App. Phys.* **2009**, *105*, 033719.

(26) Ivanovskii, A. L.; Shein, I. R.; Makurin, Yu. N.; Kiiko, V. S.; Gorbunova, M. A. *Inorg. Mater.* **2009**, *45*, 223.
(27) Sorokin, P. B.; Fedorov, A. S.; Chernozatonskiĭ, L. A. *Phys. Solid State* **2006**, *48*, 398.
(28) Vidal-Valat, G.; Vidal, J. P.; Kurki-Suonio, K.; Kurki-Suonio, R. *Acta Crystallogr., Sect. A* **1987**, *43*, 540.
(29) Baumeier, B.; Krüger, P.; Pollmann, J. *Phys. Rev. B* **2007**, *76*, 085407.
(30) Chang, K. J.; Cohen, M. L. *Solid State Commun.* **1984**, *50*, 487.
(31) Smith, D. K.; Cline, C. F.; Austerman, S. B. *Acta Crystallogr.* **1965**, *18*, 393.
(32) Continenza, A.; Wentzcovitch, R. M.; Freeman, A. J. *Phys. Rev. B* **1990**, *41*, 3540.
(33) Ijchanot, A.; Baraille, I.; Larrieu, C.; Chaillet, M. *Phys. Rev. B* **1995**, *52*, 17480.
(34) Gorbunova, M. A.; Shein, I. R.; Makurin, Yu. N.; Ivanovskaya, V. V.; Kijko, V. S.; Ivanovskii, A. L. *Physica E* **2008**, *41*, 164.
(35) Zhang, Y.; Tan, Y. W.; Stormer, H. L.; Kim, P. *Nature* **20054**, *38*, 201.
(36) Kresse, G.; Furthmuller, J. *Phys. Rev. B* **1996**, *54*, 11169.
(37) Vanderbilt, D. *Phys. Rev. B* **1990**, *41*, 7892.
(38) Neugebauer, J.; Scheffler, M. *Phys. Rev. B* **1992**, *46*, 16067.
(39) Topsakal, M.; Cahangirov, S.; Bekaroglu, E.; Ciraci, S. *Phys. Rev. B* **2009**, *80*, 235119.
(40) Botello-Méndez, A. R.; López-Urías, F.; Terrones, M.; Terrones, H. *Nano Lett.* **2008**, *8*, 1562.
(41) Peng, H.; Xiang, H. J.; Wei, S.; Li, S.; Xia, J.; Li, J. *Phys. Rev. Lett.* **2009**, *102*, 017201.